INTERNATIONAL JOURNAL FOR NUMERICAL METHODS IN FLUIDS, VOL. 19, 207–236 (1994)

FINITE ELEMENT ANALYSIS OF THE AXIALLY SYMMETRIC MOTION OF AN INCOMPRESSIBLE VISCOUS FLUID IN A SPHERICAL ANNULUS

W. NI AND N. J. NIGRO*

Dept of Mechanical and Industrial Engineering, Marquette University, Milwaukee, WI 53233, U.S.A.

SUMMARY

This paper presents results obtained by employing a modified Galerkin finite element method to analyse the steady state flow of a fluid contained between two concentric, rotating spheres. The spheres are assumed to be rigid and the cavity region between the spheres is filled with an incompressible, viscous, Newtonian fluid. The inner sphere is constrained to rotate about a vertical axis with a prescribed angular velocity, while the outer sphere is fixed. Results for the circumferential function Ω, streamfunction Ψ, vorticity function ζ and inner boundary torque T_1 are presented for Reynolds numbers $Re \leqslant 2000$ and radius ratios $0{\cdot}1 \leqslant \alpha \leqslant 0{\cdot}9$. The method proved effective for obtaining results for a wide range of radius ratios ($0{\cdot}1 \leqslant \alpha \leqslant 0{\cdot}9$) and Reynolds numbers ($0 \leqslant Re \leqslant 2000$). Previous investigators who employed the finite difference method experienced difficulties in obtaining results for cases with radius ratios $\alpha \leqslant 0{\cdot}2$, except for small Reynolds numbers ($Re \leqslant 100$). Results for Ω, Ψ, ζ and T_1 obtained in this study for radius ratios $0{\cdot}8 < \alpha < 0{\cdot}9$ verified the development of Taylor vortices reported by other investigators. The research indicates that the method may be useful for analysing other non-linear fluid flow problems.

KEY WORDS Finite element Fluid flow Rotating sphere

INTRODUCTION

The problem involving the motion of a viscous, incompressible fluid contained between two concentric spheres rotating about a common axis with prescribed angular velocities and/or torques has been the subject of extensive research in engineering, meteorology and geophysics. Previous investigators have employed various methods to study this problem. Experimental studies on boundary torques and fluid stability for the problem involving the steady state flow of a fluid in a gap between two spheres with prescribed angular velocities have been conducted by Sorokin *et al.*,[1], Khlebutin,[2] Zierep and Sawatzki,[3] Munson and Menguturk,[4] Wimmer,[5,6] Buhler,[7,8] Yavorskaya *et al.*,[9] Nakabayashi[10] and Waked and Munson.[11,12] These studies indicated that the onset of stability is affected by the radius ratio as well as the Reynolds number.

Several investigators have studied this problem with the use of analytical methods. Proudman,[13] Stewartson[14] and Carrier[15] employed a singular perturbation method to solve the steady state problem involving the flow between two spheres which are rotating about the same axis with nearly the same angular velocities. Their boundary layer solution is valid for large Reynolds numbers. Munson and Joseph[16] employed a high-order perturbation method to solve the steady state problem between two spheres rotating with different angular velocities. Their solution is

* Author to whom correspondence should be addressed.

CCC 0271–2091/94/150207–30

Received May 1993
Revised January 1994

valid for Reynolds numbers $Re \leqslant 1000$ and a radius ratio $\alpha = 0{\cdot}5$. Gagliardi *et al.*[17] also employed this method to obtain results for both the steady state and transient cases. These results are valid for $Re \leqslant 100$ and $0{\cdot}2 \leqslant \alpha \leqslant 0{\cdot}9$.

Haberman[18] also solved this problem with an analytical method by employing the primary solution[19] for the circumferential function Ω and approximating the equation for the streamfunction Ψ. His solution is valid for small Reynolds numbers and $0 \leqslant \alpha \leqslant 0{\cdot}9$. Dennis and Singh[20] extended this work by using a series method to reduce the fluid equations to a system of ordinary differential equations. They solved these equations numerically for $Re \leqslant 2000$ and $\alpha = 0{\cdot}5$. Gulwadi and Elkouh[21] developed an iterative series method to solve the problem of unsteady laminar flow in the annulus. Their results are valid for $Re \leqslant 100$ and $\alpha \leqslant 1$. Marcus and Tuckerman[22,23] applied a pseudospectral numerical method to solve the steady state and transition problems with $\alpha = 0{\cdot}85$. These results indicated the development of flow with zero, one and two Taylor vortices when the Reynolds number reached a critical value ($Re = 650$).

The vast majority of investigators who studied this problem employed the finite difference method. Pearson[24,25] obtained results for cases in which one (or both) of the spheres is given an impulsive change in angular velocity, starting from a state of either rest or uniform rotation. His results are valid for $Re \leqslant 1500$ and $\alpha = 0{\cdot}5$. Greenspan[26] and Schultz and Greenspan[27] obtained results which are valid for $Re \leqslant 3000$ and $\alpha = 0{\cdot}5$. Schrauf[28] applied this method to the narrow gap problem ($\alpha = 0{\cdot}85$). His results are valid for $Re \leqslant 2100$. Dennis and Quartapelle[29] applied a fourth-order finite difference method and obtained results which are valid for $Re \leqslant 1500$ and $0{\cdot}5 \leqslant \alpha \leqslant 0{\cdot}85$. Schwengels *et al.*[30] employed a second-order finite difference method and obtained results which are valid for $Re \leqslant 3000$ and $\alpha = 0{\cdot}5$.

Krause and Bartels[31] applied the finite difference method to study the transient flow in a spherical annulus where the inner sphere is started suddenly and the outer one is at rest. They obtained results for $Re \leqslant 14000$ and $0{\cdot}85 \leqslant \alpha \leqslant 0{\cdot}975$. Yang *et al.*[32] also employed this method to analyse the transient flow of a fluid between two spheres which are started suddenly by the action of prescribed torques. They presented results for $Re \leqslant 3000$ and $0{\cdot}2 \leqslant \alpha \leqslant 0{\cdot}9$. Lin[33] applied this method to study the motion of the fluid in an annulus between two rotating and precessing spheres. He obtained results for $Re \leqslant 100$ and $0{\cdot}5 \leqslant \alpha \leqslant 0{\cdot}9$.

In the 1960s investigators began to employ the Galerkin finite element method to solve fluid flow problems involving steady, inviscid, incompressible flow governed by Laplace's equation. Baker,[34–36] Cheng,[37] Chung,[38] Oden and co-workers[39–42] and Olson[43] were among the first to apply this method to the general fluid flow problem. A survey of this early research can be found in References 44–46. However, to date, only Bar-Yoseph *et al.*[47] have applied the finite element method to the problem of fluid flow between two rotating spheres. They formulated the fluid equations in terms of the pressure and velocity variables and applied the conventional Galerkin finite element method. Their solution is valid for $Re \leqslant 1000$ and $\alpha = 0{\cdot}5$.

In general, the analytical and finite difference methods which have been employed by previous investigators to solve this problem have not been effective for obtaining results for wide radius ratios ($\alpha < 0{\cdot}5$), except for small Reynolds numbers ($Re \leqslant 100$), and for narrow gap cases ($0{\cdot}8 < \alpha < 0{\cdot}9$) for computing the onset of Taylor vortices. Moreover, these methods are not suitable for extension to flow problems with non-spherical cavities. This limitation is overcome by the finite element method; however, the conventional Galerkin finite element method has not been employed (extensively) in the past owing to difficulties stemming from integration of the non-linear fluid flow equations. This difficulty is overcome by the modified Galerkin finite element method which is employed in this study.

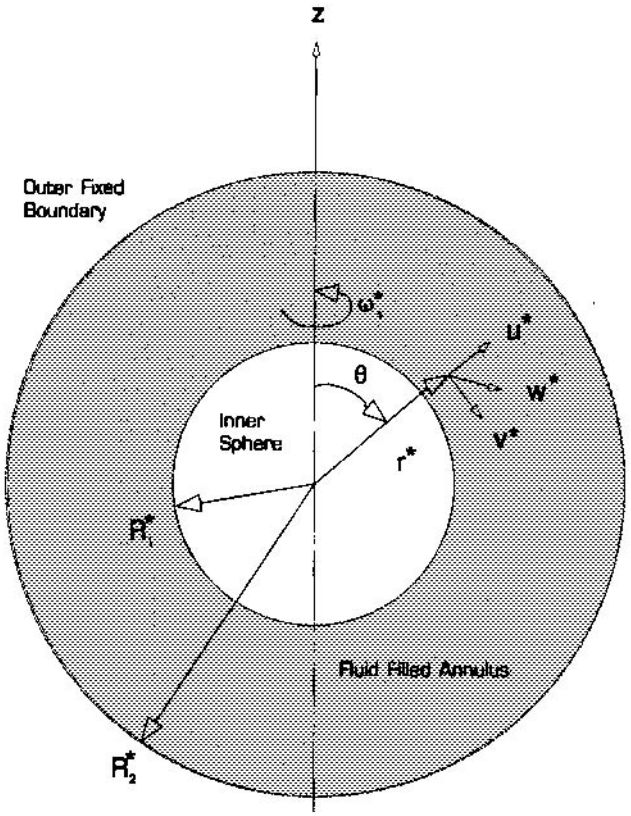

Figure 1. Notation for flow in a spherical annulus

FLUID EQUATIONS

The problem under study involves the steady state motion of an incompressible Newtonian fluid contained in an annulus between two concentric, rotating spheres (see Figure 1). The spheres are assumed to be rigid and the cavity region between the spheres is filled with a viscous fluid. The inner sphere is constrained to rotate about the vertical axis with a prescribed angular velocity, while the outer sphere is fixed. The Navier-Stokes equations are developed in spherical form and the pressure variable is eliminated by employing the streamfunction formulation. The velocity components are defined as

$$u^* = \frac{1}{r^{*2}\sin\theta}\frac{\partial \Psi^*}{\partial \theta}, \qquad v^* = -\frac{1}{r^*\sin\theta}\frac{\partial \Psi^*}{\partial r^*}, \qquad w^* = \frac{\Omega^*}{r^*\sin\theta}, \tag{1}$$

where u^* is the velocity component in the radial direction, v^* is the velocity component in the meridional direction, w^* is the velocity component in the circumferential direction, Ψ^* is the streamfunction and Ω^* is the circumferential function.

Substitution of equation (1) into the Navier–Stokes equations, introduction of the vorticity variable ζ^* and transformation to dimensionless form yields

$$D^2\Omega + Re\,\frac{\Psi_r\Omega_\theta - \Psi_\theta\Omega_r}{r^2\sin\theta} = 0, \tag{2a}$$

$$\frac{2\,Re\Omega}{r^3\sin^2\theta}(\Omega_r r\cos\theta - \Omega_\theta\sin\theta) - \frac{Re}{r^2\sin\theta}(\Psi_r\zeta_\theta - \Psi_\theta\zeta_r)$$

$$+\frac{2Re\zeta}{r^3\sin^2\theta}(\Psi_r r\cos\theta - \Psi_\theta\sin\theta) - D^2\zeta = 0, \tag{2b}$$

$$\zeta - D^2\Psi = 0, \tag{2c}$$

where

$$r = r^*/R_2^*, \qquad \Psi = \Psi^*/\omega_1^* R_2^{*3}, \qquad \Omega = \Omega^*/\omega_1^* R_2^{*2}, \qquad \zeta = \zeta^*/\omega_1^* R_2^*,$$

R_2^* is the radius of the outer sphere, ω_1^* is the angular velocity of the inner sphere, $R_e = \omega_1^* R_2^{*2}/\nu^*$ is the Reynolds number and

$$D^2 = \frac{\partial^2}{\partial r^2} + \frac{1}{r^2}\frac{\partial^2}{\partial\theta^2} - \frac{\cot\theta}{r^2}\frac{\partial}{\partial\theta}.$$

The dimensionless boundary torques are

$$T_i = \frac{3}{2}\int_0^{\pi/2}\left[r\left(r\frac{\partial\Omega}{\partial r} - 2\Omega\right)\right]\Bigg|_{r=R_i}\sin\theta\,d\theta \quad (i = 1, 2), \tag{3a}$$

where

$$T_i = -T_i^*/\tfrac{8}{3}\pi\rho_f^*\nu^*\omega_1^* R_2^{*3}, \tag{3b}$$

ρ_f^* is the density of the fluid and $R_i = R_i^*/R_2^*$.

The dimensionless symmetry and boundary conditions are given respectively as

$$\Psi(r, 0) = \Psi(r, \pi/2) = \Psi(r_1\,\theta) = \Psi(r_2, \theta) = 0, \tag{4a}$$

$$\frac{\partial}{\partial r}\Psi(r, 0) = \frac{\partial}{\partial r}\Psi(r, \pi/2) = \frac{\partial}{\partial r}\Psi(r_1, \theta) = \frac{\partial}{\partial r}\Psi(r_2, \theta) = 0, \tag{4b}$$

$$\frac{\partial}{\partial\theta}\Psi(r, 0) = \frac{\partial}{\partial\theta}\Psi(r_2, \theta) = \frac{\partial}{\partial\theta}\Psi(r_1, \theta) = 0 \tag{4c}$$

and

$$\Omega(r, 0) = 0, \tag{4d}$$

$$\Omega(r_1, \theta) = w_1 r_1^2\sin^2\theta, \tag{4e}$$

$$\Omega(r_2, \theta) = w_2 r_2^2\sin^2\theta, \tag{4f}$$

$$\frac{\partial}{\partial r}\Omega(r, 0) = \frac{\partial}{\partial\theta}\Omega(r, 0) = \frac{\partial}{\partial\theta}\Omega(r, \pi/2) = 0, \tag{4g}$$

$$\frac{\partial}{\partial\theta}\Omega(r_1, \theta) = 2w_1 r_1^2 \sin\theta\cos\theta, \tag{4h}$$

$$\frac{\partial}{\partial\theta}\Omega(r_2, \theta) = 2w_2 r_2^2 \sin\theta\cos\theta, \tag{4i}$$

$$\zeta(r, 0) = 0, \tag{4j}$$

$$\zeta(r, \pi/2) = 0, \tag{4k}$$

$$\frac{\partial}{\partial r}\zeta(r, 0) = 0, \tag{4l}$$

$$\frac{\partial}{\partial r}\zeta(r, \pi/2) = 0, \tag{4m}$$

$$R_1 < r < R_2. \tag{4n}$$

MODIFIED FINITE ELEMENT METHOD

Finite element mesh

In order to apply the finite element method, the field domain is discretized with a uniform mesh of finite elements as shown in Figure 2. The discretized values for r_i and θ_j are defined as

$$r_i = (i-1)\Delta r + R_{12} \quad \text{for } i = 1, 2, \ldots, I+1, \tag{5a}$$

$$\theta_j = (j-1)\Delta\theta \quad \text{for } j = 1, 2, \ldots, J+1, \tag{5b}$$

where I is the number of divisions in the r-direction, J is the number of divisions in the θ-direction,

$$\Delta r = (1 - R_{12})/I, \tag{5c}$$

$$R_{12} = R_1^*/R_2^*, \tag{5d}$$

$$\Delta\theta = \pi/2J. \tag{5e}$$

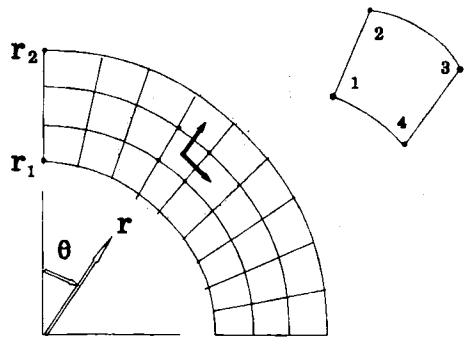

Figure 2. Finite element mesh

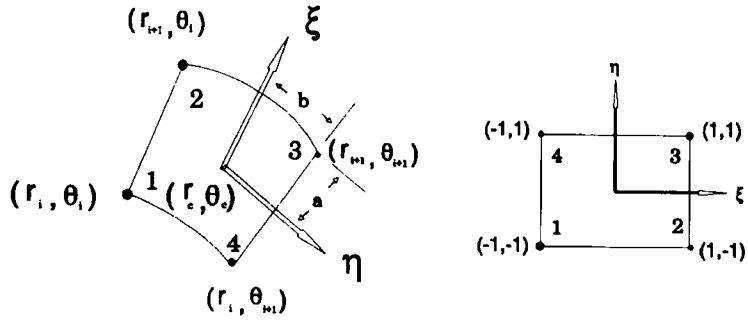

Figure 3. Transformation of element co-ordinates

The polar elements are transformed into four-node rectangular elements as shown in Figure 3. The relationships between the dimensionless rectangular element co-ordinates (ξ, η) and the polar nodal co-ordinates (r_i, θ_j) are

$$\xi = \frac{1}{a}(r - r_c), \tag{6a}$$

$$\eta = \frac{1}{b}(\theta - \theta_c). \tag{6b}$$

The number of elements is given by the equation

$$N = N_r \times N_\theta, \tag{7a}$$

where N is the total number of elements, N_r is the number of increments in the r-direction and N_θ is the number of increments in the θ-direction. The element aspect ratio is defined as

$$\gamma = L_\theta^{(e)}/L_r^{(e)}, \tag{7b}$$

where γ is the aspect ratio, $L_\theta^{(e)}$ is the uniform dimensionless length of the element in the θ-direction and $L_r^{(e)}$ is the uniform dimensionless length of the element in the r-direction.

Interpolation functions

The field variables are expanded over each element as

$$\Omega^{(e)} = \sum_{i=1}^{12} \alpha_i \Omega_i, \tag{8a}$$

$$\zeta^{(e)} = \sum_{i=1}^{12} \alpha_i \zeta_i, \tag{8b}$$

$$\Psi^{(e)} = \sum_{i=1}^{12} \alpha_i \Psi_i, \tag{8c}$$

where α_i are element interpolation functions,

$$\alpha_1 = \tfrac{1}{8}(\xi - 1)(\eta - 1)(2 - \eta - \xi - \eta^2 - \xi^2), \tag{9a}$$

$$\alpha_2 = \tfrac{1}{8}(\xi + 1)(\eta - 1)(-2 + \eta - \xi + \eta^2 + \xi^2), \tag{9b}$$

$$\alpha_3 = \tfrac{1}{8}(\xi + 1)(\eta + 1)(2 + \eta + \xi - \eta^2 - \xi^2), \tag{9c}$$

$$\alpha_4 = \tfrac{1}{8}(\xi - 1)(\eta + 1)(-2 - \eta + \xi + \eta^2 + \xi^2), \tag{9d}$$

$$\alpha_5 = -\tfrac{1}{8}(\eta - 1)(\xi - 1)^2(\xi + 1), \tag{9e}$$

$$\alpha_6 = -\tfrac{1}{8}(\eta - 1)(\xi + 1)^2(\xi - 1), \tag{9f}$$

$$\alpha_7 = \tfrac{1}{8}(\eta + 1)(\xi + 1)^2(\xi - 1), \tag{9g}$$

$$\alpha_8 = \tfrac{1}{8}(\eta + 1)(\xi - 1)^2(\xi + 1), \tag{9h}$$

$$\alpha_9 = -\tfrac{1}{8}(\eta - 1)^2(\xi - 1)(\eta + 1), \tag{9i}$$

$$\alpha_{10} = \tfrac{1}{8}(\eta - 1)^2(\xi + 1)(\eta + 1), \tag{9j}$$

$$\alpha_{11} = \tfrac{1}{8}(\eta + 1)^2(\xi + 1)(\eta - 1), \tag{9k}$$

$$\alpha_{12} = -\tfrac{1}{8}(\eta + 1)^2(\xi - 1)(\eta - 1), \tag{9l}$$

$\Omega_i, \zeta_i, \Psi_i$ $(i = 1, 2, \ldots, 12)$ are nodal co-ordinates, $\Omega_i, \zeta_i, \Psi_i$ $(i = 1, 2, 3, 4)$ are nodal variables, $\Omega_i, \zeta_i, \Psi_i$ $(i = 5, 6, 7, 8)$ are nodal derivatives with respect to $\xi = (\partial\Omega_{i-4}/\partial\xi, \partial\zeta_{i-4}/\partial\xi, \partial\Psi_{i-4}/\partial\xi)$ and $\Omega_i, \zeta_i, \Psi_i$ $(i = 9, 10, 11, 12)$ are nodal derivatives with respect to $\eta = (\partial\Omega_{i-8}/\partial\eta, \partial\zeta_{i-8}/\partial\eta, \partial\Psi_{i-8}/\partial\eta)$.

Finite element equations

The fluid equations are reduced to algebraic form by employing a modification of the conventional Galerkin finite element method.[45] With the conventional method the finite element equations are obtained by first integrating the Galerkin variational form with the aid of Green's theorem. This can lead to difficulty in the case of non-linear boundary value problems. Cheng[37] circumvented this problem by linearizing the transient fluid flow equation at each time step before performing the integration by parts. He obtained the steady state solution from the asymptotic solution of the transient problem.

In this research the nodal co-ordinates given in equations (8) are selected such that all the symmetry and boundary conditions (equations (4)) are automatically satisfied. The finite element equations are obtained directly from the Galerkin variational form without integration by parts. The variational form for this fluid flow problem is[48]

$$\int f_1^{(e)} \delta\Omega^{(e)} \, dR = 0, \tag{10a}$$

$$\int f_2^{(e)} \delta\Psi^{(e)} \, dR = 0, \tag{10b}$$

$$\int f_3^{(e)} \delta\zeta^{(e)} \, dR = 0, \tag{10c}$$

where f_1, f_2 and f_3 are as defined in equations (2a)–(2c) respectively.

The finite element equations for the interior element are obtained by substituting equations (8) into equations (10) to yield

$$\int f_1^{(e)}\alpha_i^{(e)}\,dR = 0, \tag{11a}$$

$$\int f_2^{(e)}\alpha_i^{(e)}\,dR = 0, \tag{11b}$$

$$\int f_3^{(e)}\alpha_i^{(e)}\,dR = 0, \tag{11c}$$

where $i = 1, 2, 3, \ldots, 12$.

The finite element equations for the boundary elements are obtained by replacing the appropriate equations in (11) with the actual nodal boundary conditions which satisfy equations (4). Substitution of equations (2) into equations (11) yields

$$A_i^{(e)} = \int \left[\frac{Re}{r^{*2}\sin\theta}\left\{\sum_{l=1}^{12}\left[\sum_{n=1}^{12}\left(\frac{\partial\alpha_n}{\partial r}\frac{\partial\alpha_l}{\partial\theta} - \frac{\partial\alpha_n}{\partial\theta}\frac{\partial\alpha_l}{\partial r}\right)\Psi_n\right]\Omega_l\right\}\right.$$
$$\left. + \sum_{l=1}^{12}\left(\frac{\partial^2\alpha_l}{\partial r^2} + \frac{1}{r^2}\frac{\partial^2\alpha_l}{\partial\theta^2} - \frac{\cot\theta}{r^2}\frac{\partial\alpha_l}{\partial\theta}\right)\Omega_l\right]\alpha_i\,dR = 0, \tag{12a}$$

$$B_i^{(e)} = \int \left\{\frac{2Re}{r^3\sin^2\theta}\left(\sum_{l=1}^{12}\alpha_l\Omega_l\right)\sum_{l=1}^{12}\left(r\cos\theta\frac{\partial\alpha_l}{\partial r} - \sin\theta\frac{\partial\alpha_l}{\partial\theta}\right)\Omega_l\right.$$
$$- \frac{Re}{r^2\sin\theta}\sum_{n=1}^{12}\left[\sum_{n=1}^{12}\left(\frac{\partial\alpha_n}{\partial r}\frac{\partial\alpha_m}{\partial\theta} - \frac{\partial\alpha_n}{\partial\theta}\frac{\partial\alpha_m}{\partial r}\right)\Psi_n\right]\zeta_m$$
$$+ \frac{2Re}{r^3\sin^2\theta}\left(\sum_{m=1}^{12}\alpha_m\zeta_m\right)\sum_{n=1}^{12}\left(r\cos\theta\frac{\partial\alpha_n}{\partial r} - \sin\theta\frac{\partial\alpha_n}{\partial\theta}\right)\Psi_n$$
$$\left. - \sum_{m=1}^{12}\left(\frac{\partial^2\alpha_m}{\partial r^2} + \frac{1}{r^2}\frac{\partial^2\alpha_m}{\partial\theta^2} - \frac{\cot\theta}{r^2}\frac{\partial\alpha_m}{\partial\theta}\right)\zeta_m\right\}\alpha_i\,dR = 0, \tag{12b}$$

$$C_i^{(e)} = \int\left[\sum_{m=1}^{12}\alpha_m\zeta_m - \sum_{n=1}^{12}\left(\frac{\partial^2\alpha_n}{\partial r^2} + \frac{1}{r^2}\frac{\partial^2\alpha_n}{\partial\theta^2} - \frac{\cot\theta}{r^2}\frac{\partial\alpha_n}{\partial\theta}\right)\Psi_n\right]\alpha_i\,dR = 0, \tag{12c}$$

where $i = 1, 2, 3, \ldots, 12$.

Method of analysis

The element equations (12) are assembled and then solved by employing the following procedure.

1. The element equations are linearized before assembly by employing a Taylor series expansion about a base value ($\bar{\Omega}_0$, $\bar{\zeta}_0$, $\bar{\Psi}_0$). The resulting linearized finite element equations have the form

$$k^{(e)}\Delta\bar{q}^{(e)} = -\bar{g}^{(e)}, \tag{13}$$

where

$$\bar{q}^{(e)} = (\bar{q}_i^{(e)}) \quad (i = 1, 2, \ldots, 36)$$
$$= (\bar{\Omega}^{(e)}, \bar{\zeta}^{(e)}, \bar{\Psi}^{(e)}),$$

$$\Delta\bar{q}^{(e)} = (\Delta\bar{\Omega}^{(e)}, \Delta\bar{\zeta}^{(e)}, \Delta\bar{\Psi}^{(e)}),$$

$$\bar{g}^{(e)} = (\bar{A}^{(e)}, \bar{B}^{(e)}, \bar{C}^{(e)}), \qquad k^{(e)} = (k_{ij}^{(e)}),$$

$$(k_{ij}^{(e)}) = \left(\frac{\partial A_i^{(e)}}{\partial q_j^{(e)}}\right) \quad (i = 1, 2, \ldots, 12) \quad (j = 1, 2, \ldots, 36), \tag{14a}$$

$$(k_{ij}^{(e)}) = \left(\frac{\partial C_i^{(e)}}{\partial q_j^{(e)}}\right) \quad (i = 13, 14, \ldots, 24) \quad (j = 1, 2, \ldots, 36), \tag{14b}$$

$$(k_{ij}^{(e)}) = \left(\frac{\partial B_i^{(e)}}{\partial q_j^{(e)}}\right) \quad (i = 25, 26, \ldots, 36) \quad (j = 1, 2, \ldots, 36). \tag{14c}$$

2. The integrals in equations (12) are evaluated numerically by employing the Gauss quadrature algorithm. The linearized element equations (14) are assembled to yield

$$K\Delta\bar{Q} = -\bar{G}, \tag{15}$$

where K is the global element stiffness matrix,

$$\Delta\bar{Q} = \begin{pmatrix} \Delta\bar{\Omega} \\ \Delta\bar{\zeta} \\ \Delta\bar{\Psi} \end{pmatrix}, \qquad \bar{G} = \begin{pmatrix} \bar{A} \\ \bar{B} \\ \bar{C} \end{pmatrix}.$$

3. Equation (15) is solved iteratively by employing the Newton–Raphson algorithm

$$K^n\Delta\bar{Q}^n = -\bar{G}^n, \tag{16a}$$

$$\bar{Q}^{n+1} = \bar{Q}^n + \Delta Q^n. \tag{16b}$$

The iterative process is terminated when the norm $\|\Delta Q\|$ is less than a specified error. The process was assumed to be divergent if the error was not satisfied in five iterations. The equations were solved by employing a quasi-steady-state procedure, i.e. by increasing the values of the Reynolds numbers in small increments (e.g. $Re^1 = 0$, $Re^2 = 10$, $Re^3 = 100$, etc.), beginning with the creeping flow solution ($Re^1 = 0$). The results obtained for Re^m were used as initial estimates for the case with Reynolds numbers Re^{m+1}.

RESULTS

Case studies

The procedure described above was implemented with the use of a computer program. Results for $\bar{\Omega}$, $\bar{\Psi}$ and $\bar{\zeta}$ were obtained by running the computer programme in double precision with varying radius ratios, Reynolds numbers and mesh sizes. The values of radius ratios (α), corresponding aspect ratios (γ) and final values of N which were employed in this research are given in Table I.

Table I. Case studies

α	Number of elements (N)	Aspect ratio (γ)
0·1	4 × 8	0·87
0·2	4 × 8	0·98
0·3	4 × 8	1·12
0·44	4 × 12	0·93
0·5	4 × 12	1·05
0·6	4 × 12	1·31
0·775	2 × 24	0·58
0·8	2 × 24	0·65
0·825	2 × 24	0·75
0·85	2 × 24	0·87
0·875	2 × 24	1·05
0·9	2 × 24	1·31

Validation of modified Galerkin method

The finite element procedure was tested for convergence and accuracy by first applying it to several one- and two-dimensional linear boundary value problems. Although not shown here, the method yielded results which were in excellent agreement with those obtained from the exact solution.[48] Moreover, for a given number of elements the results were more precise than those obtained from the conventional Ritz and Galerkin methods.

The number of elements required for convergence of the Ω, Ψ, ζ, T_1 and T_2 results for the fluid problem was affected by the radius ratio (α), the number of elements (N), the aspect ratio (γ) and the Reynolds number (Re). Typical values of N which were employed to test convergence are given in Table II. For low Reynolds numbers ($Re \leqslant 100$) the solution process converged for all cases regardless of the values of N and γ.[48] However, the aspect ratio must be maintained at a value near unity in order to obtain good results for high Reynolds numbers. The results failed to converge for $\alpha = 0{\cdot}9$ and $\gamma > 2{\cdot}7$ regardless of N. In general there was a small discrepancy between the steady state results for T_1 and T_2, even though these values should be equal. This discrepancy, which increased as the Reynolds number increased and N decreased, was also noted by other investigators.[29,32]

Results for the inner torque ($-T_1$) are compared in Table III with those obtained from the creeping flow solution ($Re \to 0$) for various values of α. As can be seen from the table, the results are all in good agreement. Values of the torque ($-T_1$) were also compared with

Table II. Numbers of elements ($N = N_r \times N_\theta$) for testing convergence

$\alpha = 0{\cdot}2$	$N = 2 \times 4$ $\gamma = 0{\cdot}98$	$N = 3 \times 6$ $\gamma = 0{\cdot}98$	$N = 4 \times 8$ $\gamma = 0{\cdot}98$
$\alpha = 0{\cdot}5$	$N = 2 \times 6$ $\gamma = 1{\cdot}05$	$N = 3 \times 9$ $\gamma = 1{\cdot}05$	$N = 4 \times 12$ $\gamma = 1{\cdot}05$
$\alpha = 0{\cdot}9$	$N = 2 \times 6$ $\gamma = 5{\cdot}24$	$N = 2 \times 12$ $\gamma = 2{\cdot}62$	$N = 2 \times 24$ $\gamma = 1{\cdot}31$

Table III. Comparison of torque results ($-T_1$) with creeping flow solution

α	Creeping flow solution	This study
0·2	0·0242	0·0240
0·44	0·2794	0·2792
0·5	0·4286	0·4285
0·9	8·0701	8·0700

Table IV. Comparison of torque results ($-T_1$) with results of other investigators

Case	Dennis and Singh[20]	Dennis and Quartapelle[29]	Munson and Joseph[16]	Yang *et al.*[32]	Gagliardi *et al.*[17]	This study
$\alpha = 0{\cdot}2$, $Re = 10$	—	—	—	0·0241	0·0242	0·0240
$\alpha = 0{\cdot}2$, $Re = 100$	—	—	—	0·0244	0·0241	0·0242
$\alpha = 0{\cdot}5$, $Re = 10$	—	—	0·429	0·4287	0·427	0·4286
$\alpha = 0{\cdot}5$, $Re = 100$	0·446	0·445	0·446	0·4463	0·443	0·4483
$\alpha = 0{\cdot}5$, $Re = 500$	0·738	0·770	0·741	0·7691	—	0·7579
$\alpha = 0{\cdot}5$, $Re = 1000$	0·978	1·039	0·986	1·010	—	1·0005
$\alpha = 0{\cdot}5$, $Re = 2000$	1·285	—	—	1·390	—	1·3008
$\alpha = 0{\cdot}9$, $Re = 10$	—	—	—	8·070	8·07	8·070
$\alpha = 0{\cdot}9$, $Re = 100$	—	—	—	8·073	8·07	8·073

those obtained by other investigators who employed finite difference and perturbation methods to solve this problem. These results, which are shown in Table IV, are in good agreement for all cases. In general the results agree best with those obtained by Yang *et al.*[32] The maximum discrepancy, which occurred with $\alpha = 0{\cdot}5$ and $Re = 2000$, is less than 7%. The values of torque versus Reynolds number shown in Figure 4 are also in good agreement with those obtained by Munson and Menguturk[4] for $\alpha = 0{\cdot}44$.

Results for Ω, Ψ and ζ were compared (qualitatively) with those obtained by several other investigators.[13,25,29,32,45] Typical comparisons of the Ω and Ψ contour plots are shown in Figures 5 and 6 for $\alpha = 0{\cdot}5$ and $Re = 2000$. The agreement between the T_1, Ω, Ψ and ζ results of this study and those obtained by other investigators demonstrates the validity of the modified Galerkin method. In general this good agreement was achieved by employing a mesh which was considerably coarser than that employed with the finite difference method (e.g. 4×12 in the case of $\alpha = 0{\cdot}5$ versus 16×26[32] and 16×32[29].

Results for radius ratios $0{\cdot}1 \leqslant \alpha \leqslant 0{\cdot}775$

Very few results are available in the literature for wide radius ratios ($\alpha < 0{\cdot}2$), except for small Reynolds number ($Re \leqslant 100$).[32] Values obtained from this study for the torque ($-T_1$) versus the Reynolds number are presented in Figure 7 for $\alpha = 0{\cdot}2$. As can be seen (see also Table III), the value of $-T_1$ approaches (asymptotically) the value predicted by the creeping flow theory as the Reynolds number (Re) approaches zero. The curve is similar (qualitatively) to that shown in Figure 4 for the medium radius ratio ($\alpha = 0{\cdot}44$); however, the amplitudes

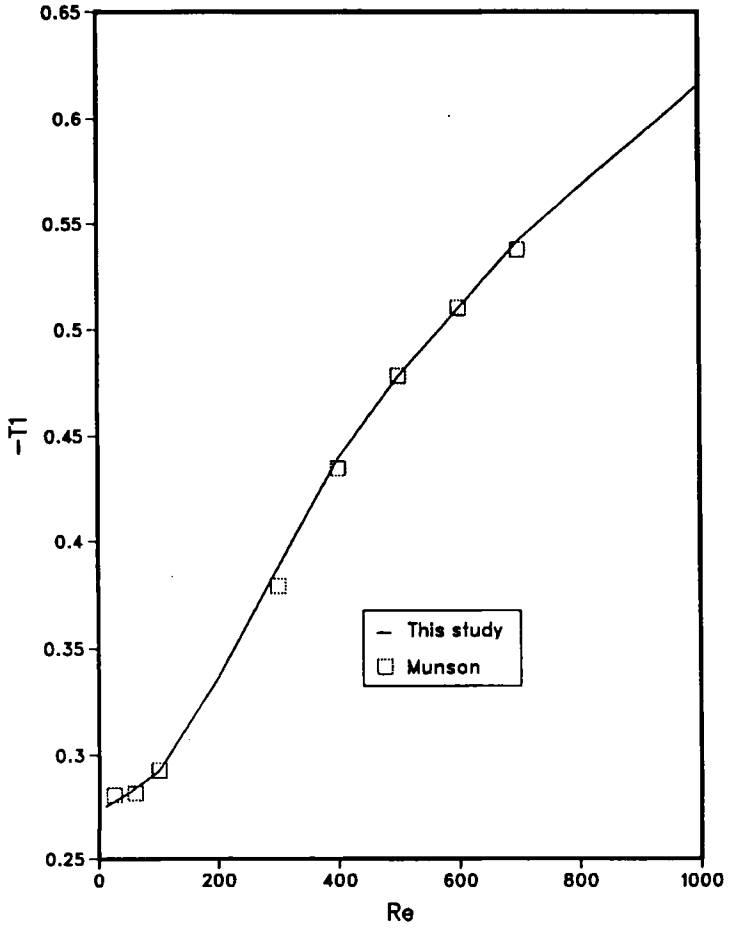

Figure 4. $-T_1$ versus Reynolds number ($\alpha = 0{\cdot}44$): —, this study; , Munson and Menguturk[4]

for corresponding values of Reynolds numbers are considerably smaller. Plots of torque ($-T_1$) versus $1/\alpha$ are shown in Figure 8 for $Re = 10, 400, 700$ and 1000. Note that these curves become tangent to the horizontal asymptotes as α approaches zero.

The Ψ contour plots with $\alpha = 0{\cdot}1$, $0{\cdot}3$, $0{\cdot}5$ and $0{\cdot}775$ are presented in Figures 9–12 for Re ranging from 100 to 1000. In this study Taylor vortices were not detected with $0{\cdot}1 \leqslant \alpha \leqslant 0{\cdot}775$ regardless of the magnitude of Re or the increment of Re used in the quasi-steady-state procedure discussed in the method of analysis section. Note that in all these plots the location of Ψ_{min} shifts slightly outwards and towards the equator ($\theta = 90°$) as Re increases. Curves showing the value of $|\Psi_{min}|$ versus α are presented in Figure 13 for $Re = 100, 500, 700$ and 1000. In general for a given Reynolds number the maximum value of $|\Psi_{min}|$ occurs in those annuli with $0{\cdot}4 < \alpha < 0{\cdot}7$. The maximum value increases with increasing Re. A plot of V_{max} (maximum magnitude of the velocity vector in the r–θ plane) versus α is shown in Figure 14. The curves in this figure agree qualitatively with those for $|\Psi_{min}|$ in Figure 13 and explain Munson and Menguturk's[4] observation that the onset of turbulent flow occurs first in annuli with medium radius ratios ($0{\cdot}5 < \alpha < 0{\cdot}7$).

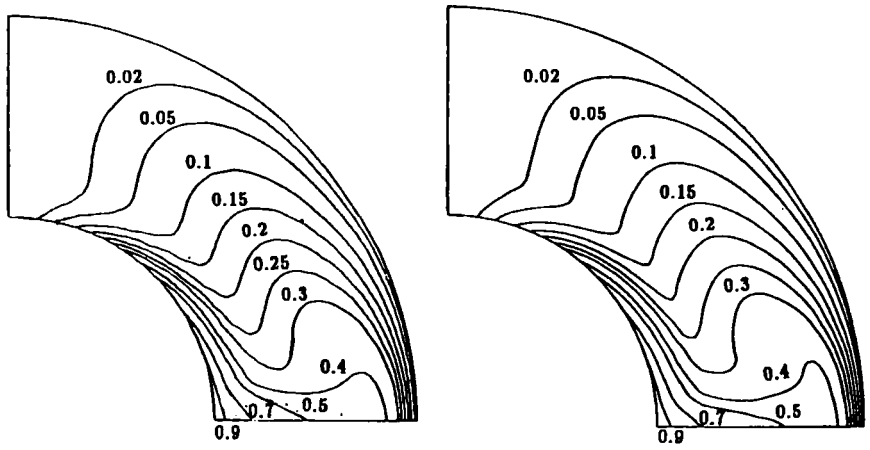

(a) Yang (N=20 × 20) (b) This study (N=4 × 12)

Figure 5. Comparison of Ω contours (Ω × 4) for $\alpha = 0{\cdot}5$ and $Re = 2000$: (a) Yang *et al.*[32] ($N = 20 \times 20$); (b) this study ($N = 4 \times 12$)

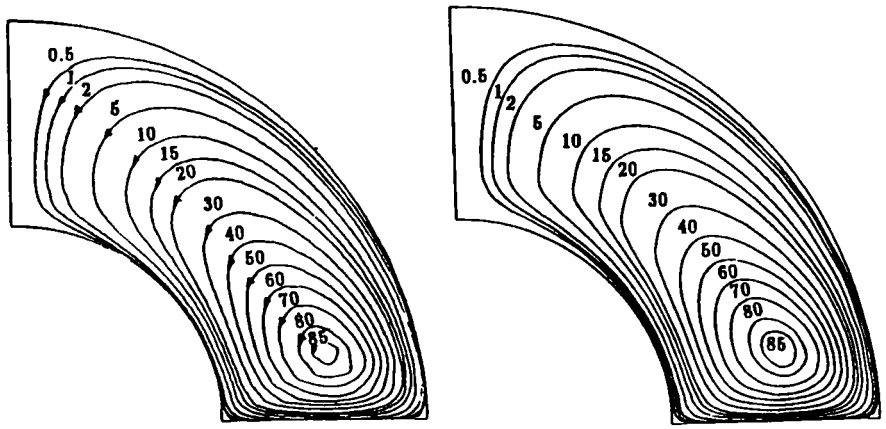

(a) Yang (N=20 × 20) (b) This study (N=4 × 12)

Figure 6. Comparison of Ψ contours ($-\Psi \times 10^4$) for $\alpha = 0{\cdot}5$ and $Re = 2000$: (a) Yang *et al.*[32] ($N = 20 \times 20$); (b) this study ($N = 4 \times 12$)

To the best of our knowledge, the only results reported in the literature[29] for vorticity are those for $\alpha = 0{\cdot}5$ and $Re = 100$. The ζ contour plots obtained from this study for $\alpha = 0{\cdot}2$ with Re ranging from 10 to 700 are presented in Figure 15. The corresponding ζ section curves at $\theta = 45°$ are shown in Figure 16. These figures indicate that the maximum (absolute) value of ζ always occurs at the surface of the inner rotating sphere. This confirms Dennis and Quartapelle's[29] conclusion that the region near the inner rotating sphere is one of intense

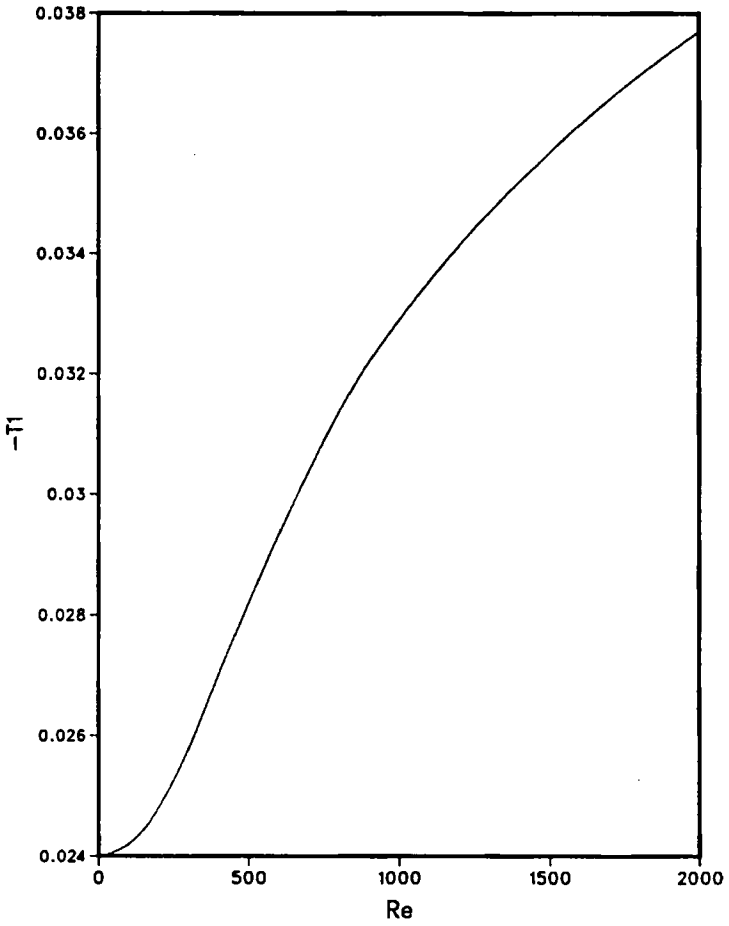

Figure 7. $-T_1$ versus Reynolds number ($\alpha = 0{\cdot}2$)

vorticity generation. The plots in Figure 16 also show that the vorticity section curves tend to become oscillatory as Re increases. The plots of ζ_{min} versus α for $Re = 10$, 100, 500 and 700 in Figure 17 indicate that for a given Reynolds number the minimum value of vorticity also occurs in those annuli with $0{\cdot}5 < \alpha < 0{\cdot}7$. Recall that this feature was also observed for the streamfunction (Ψ_{min}) and velocity (V_{max}).

Results for radius ratios $0{\cdot}775 < \alpha \leqslant 0{\cdot}9$

The Ψ contour plots obtained with $\alpha = 0{\cdot}8$, 0·825, 0·85 and 0·875 are shown in Figures 18–21. All these figures show the development of pinches (in the contour line) as the Reynolds number increases. This is followed by the development of (a) zero or one Taylor vortex when $\alpha = 0{\cdot}8$ and $Re = 700$ (Figure 18), (b) one Taylor vortex when $\alpha = 0{\cdot}825$ and $Re = 650$ (Figure 19) and when $\alpha = 0{\cdot}85$ and $Re = 750$ (Figure 20) and (c) two Taylor vortices when $\alpha = 0{\cdot}875$ and $Re = 1125$ (Figure 21). With $\alpha = 0{\cdot}8$ the development of either zero or one Taylor vortex was dependent on the increment Re employed in the solution process. Zero vortex developed when a small increment in Reynolds number ($\Delta Re = 100$) was employed starting from the

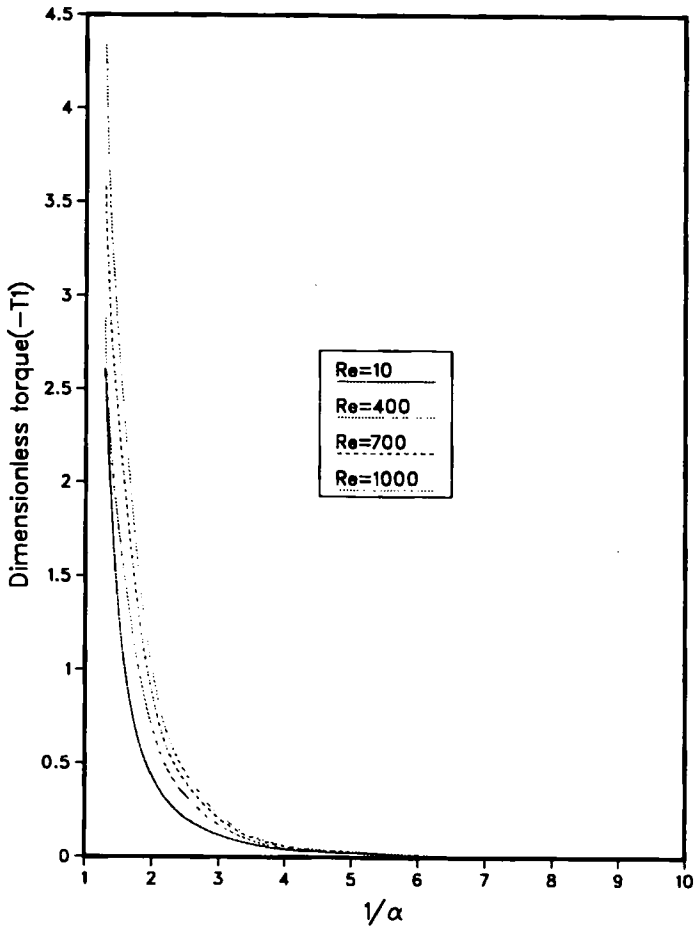

Figure 8. $-T_1$ versus reciprocal of radius ratio ($1/\alpha$)

solution with $Re = 700$. One Taylor vortex developed when a large increment in Reynolds number ($\Delta Re = 300$) was employed. Flow with two Taylor vortices did not develop with $\alpha = 0{\cdot}8$ regardless of the magnitude of ΔRe.

The results of this investigation indicate that for $\alpha = 0{\cdot}825$ and $0{\cdot}85$ only one Taylor vortex develops as the Reynolds number approaches a critical value regardless of the magnitude of ΔRe. This was also true regarding the development of two Taylor vortices when $\alpha = 0{\cdot}875$. Contour plots for Ψ with $\alpha = 0{\cdot}9$ are shown in Figure 22 for various Reynolds numbers. In general Taylor vortices did not develop for $\alpha < 0{\cdot}8$ and $\alpha > 0{\cdot}875$ regardless of the solution process. This is confirmed by the results of Buhler[7] and Marcus and Tuckerman.[22]

The inner torque values ($-T_1$) versus the Reynolds number are plotted in Figure 23 for various radius ratios. Note that for $\alpha = 0{\cdot}8$ the magnitudes of the torque corresponding to one-Taylor-vortex flow are larger than the values of the torque corresponding to zero-Taylor-vortex flow. Except for the case with $\alpha = 0{\cdot}8$, zero-Taylor-vortex flow was not observed after the critical Reynolds number regardless of the increment ΔRe used in the solution process.

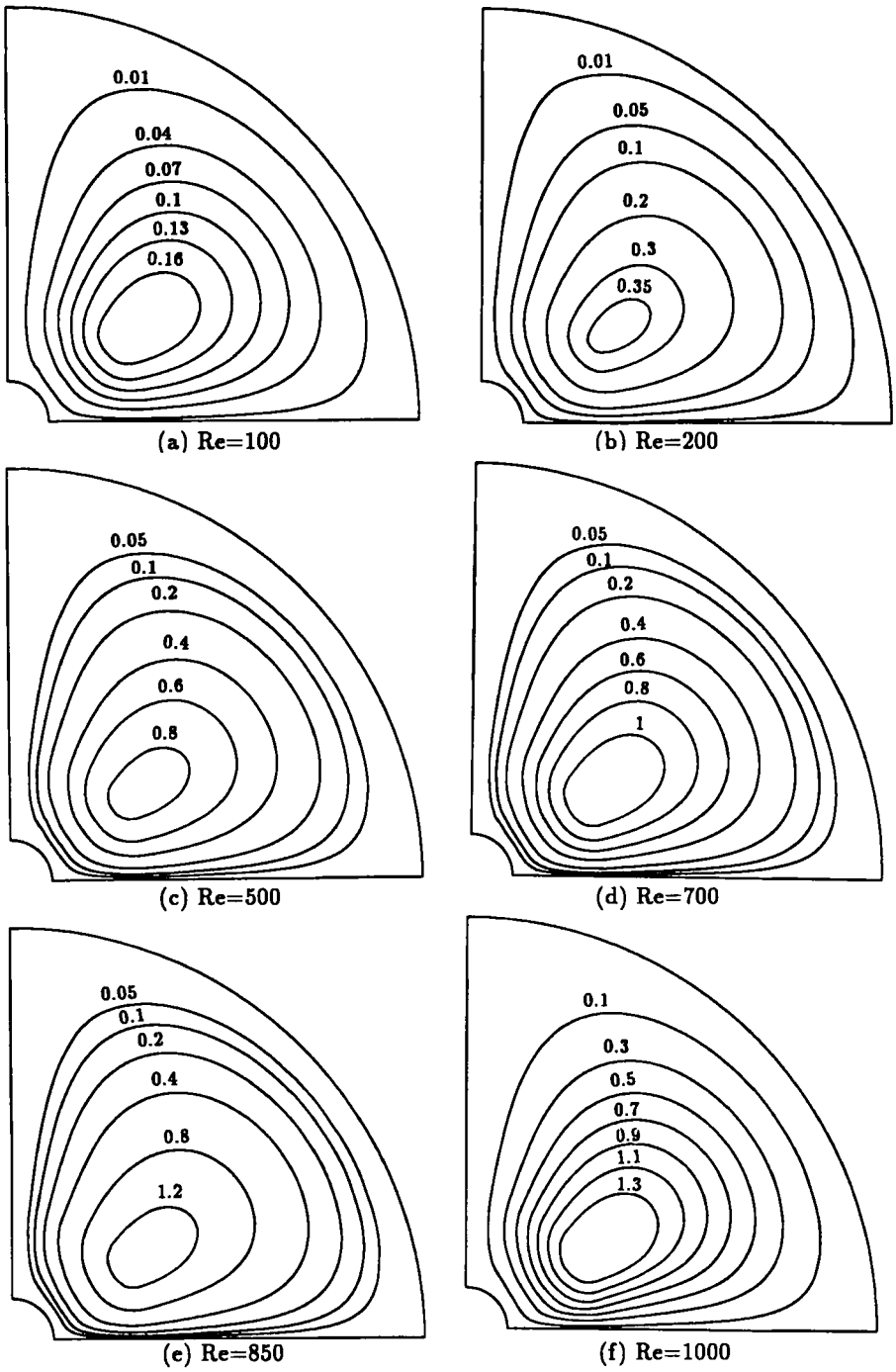

Figure 9. Contour plots of Ψ ($-\Psi \times 10^4$) for $\alpha = 0{\cdot}1$

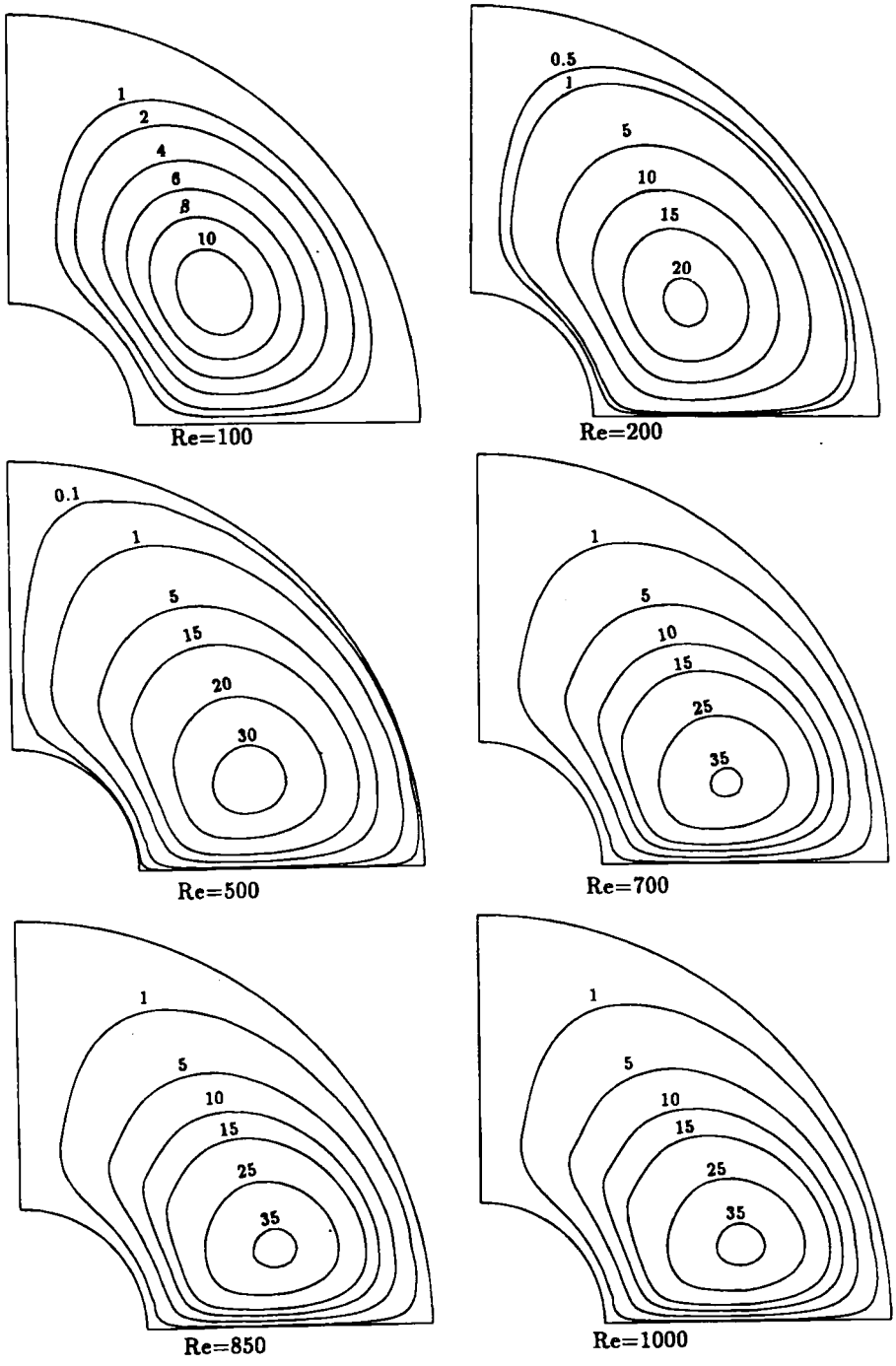

Figure 10. Contour plots of Ψ ($-\Psi \times 10^4$) for $\alpha = 0{\cdot}3$

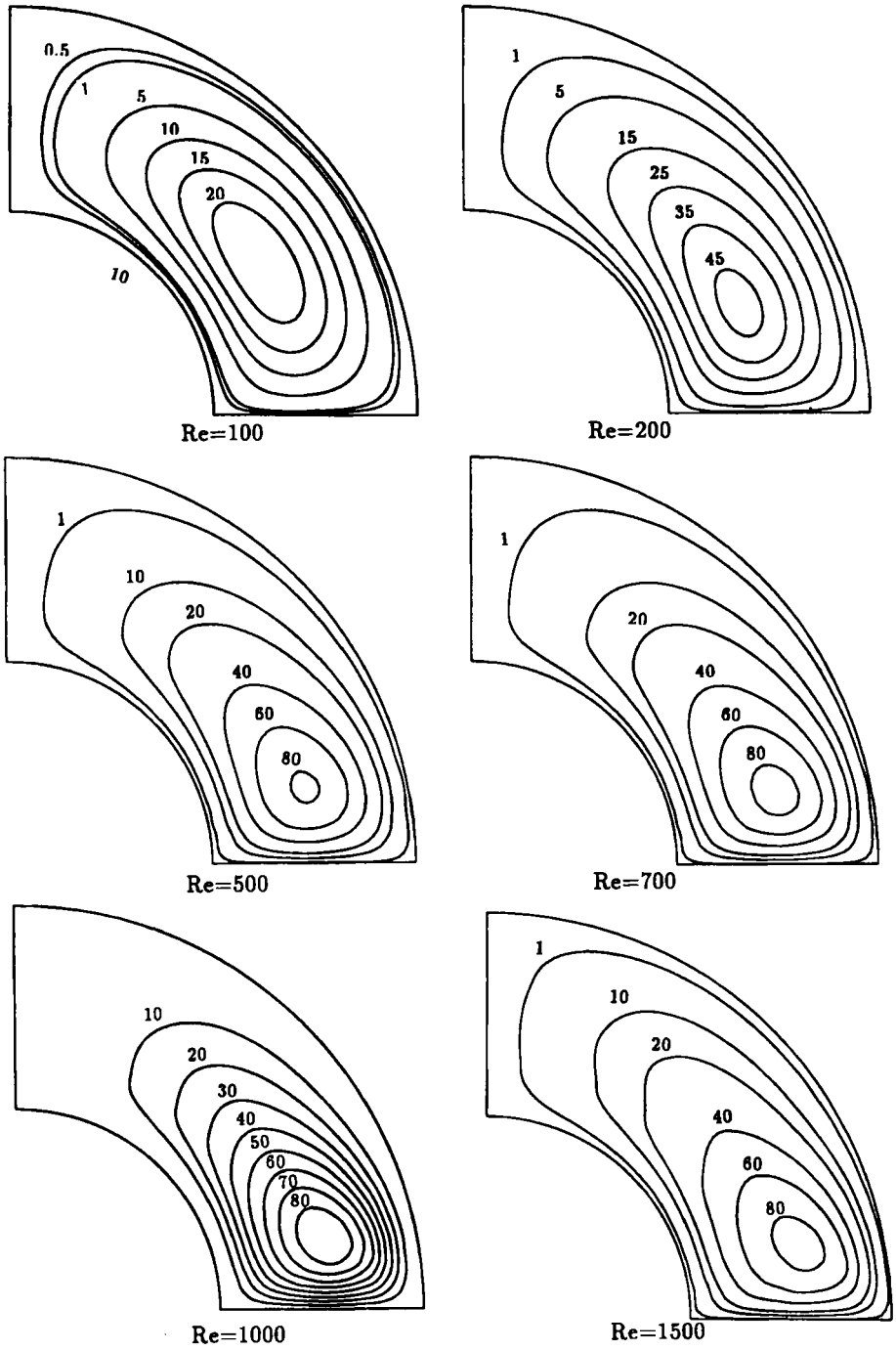

Figure 11. Contour plots of Ψ ($-\Psi \times 10^4$) for $\alpha = 0{\cdot}5$

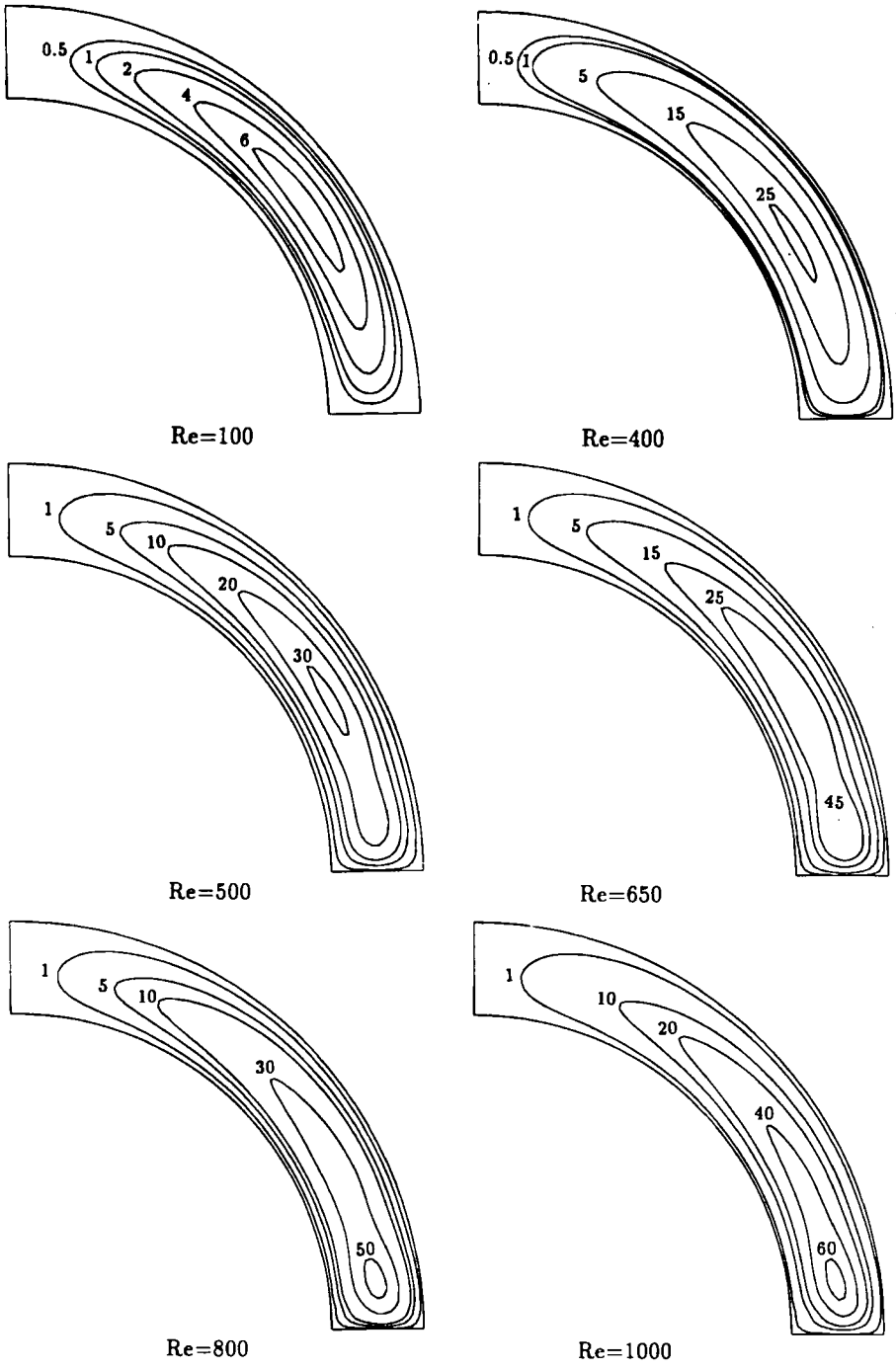

Figure 12. Contour plots of Ψ ($-\Psi \times 10^4$) for $\alpha = 0{\cdot}775$

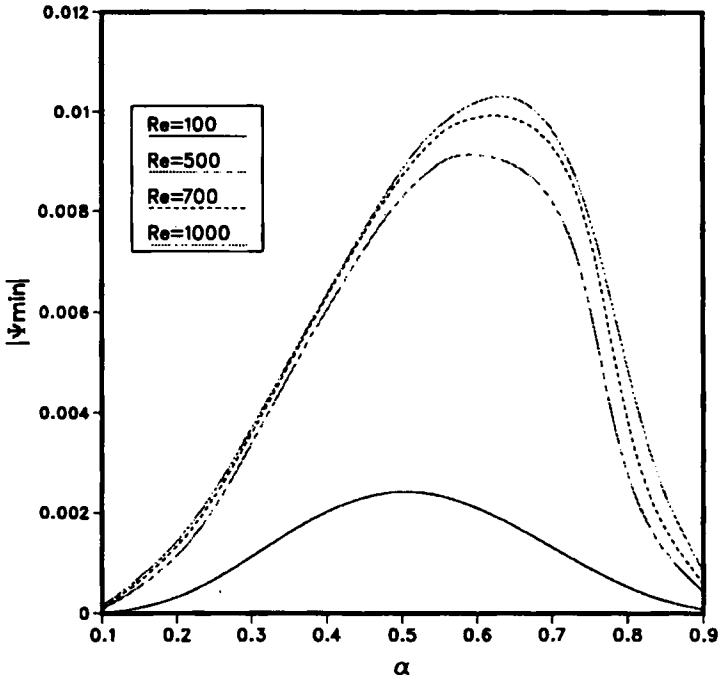

Figure 13. $|\Psi_{min}|$ versus α

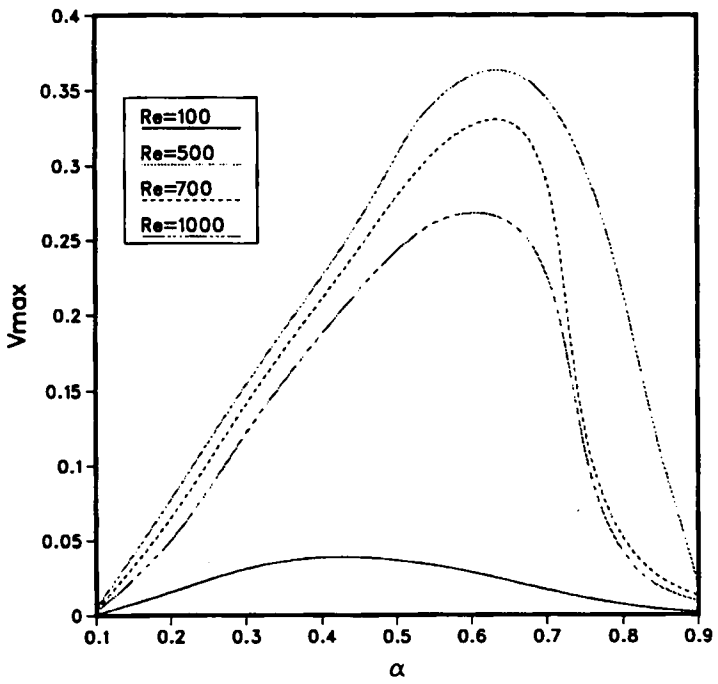

Figure 14. V_{max} versus α

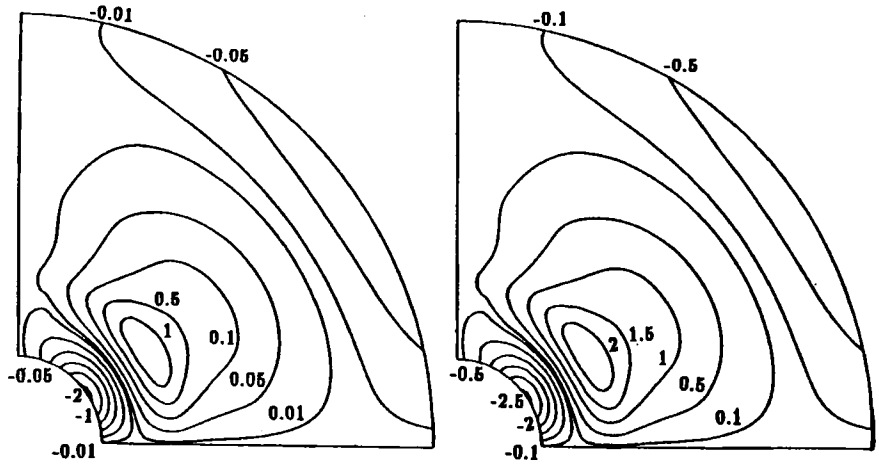

(a) $R_e = 10$ (N =4 × 12) (b) $R_e = 100$ (N =4 × 12)

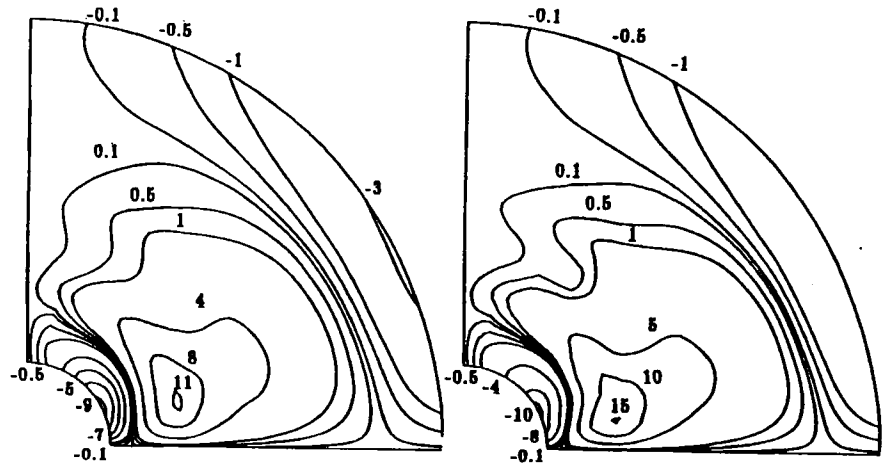

(c) $R_e = 500$ (N =4 × 12) (d) $R_e = 700$ (N =4 × 12)

Figure 15. Contour plots of ζ ($\zeta \times 10^2$) for $\alpha = 0{\cdot}2$

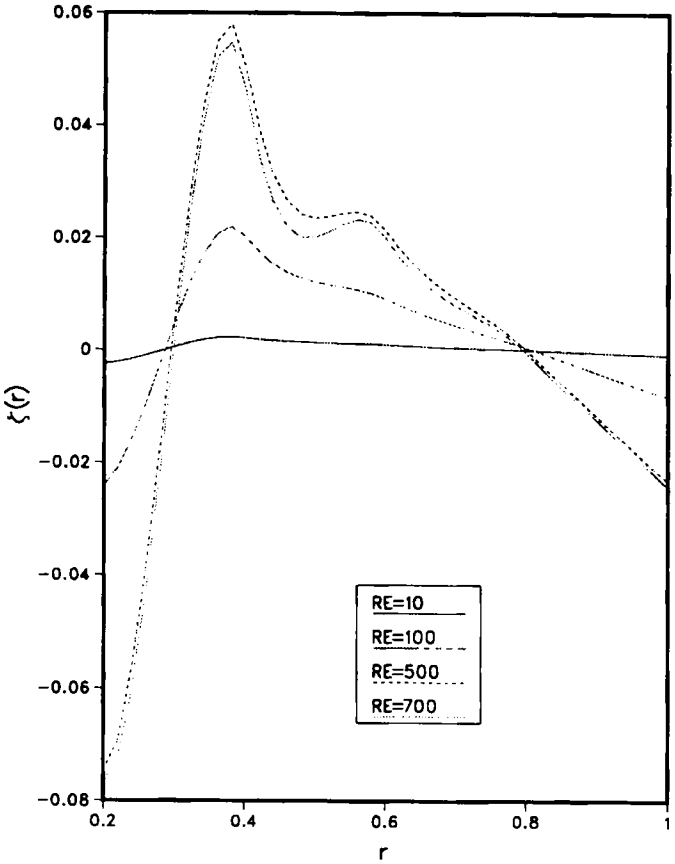

Figure 16. ζ versus r at $\theta = 45°$ ($\alpha = 0{\cdot}2$)

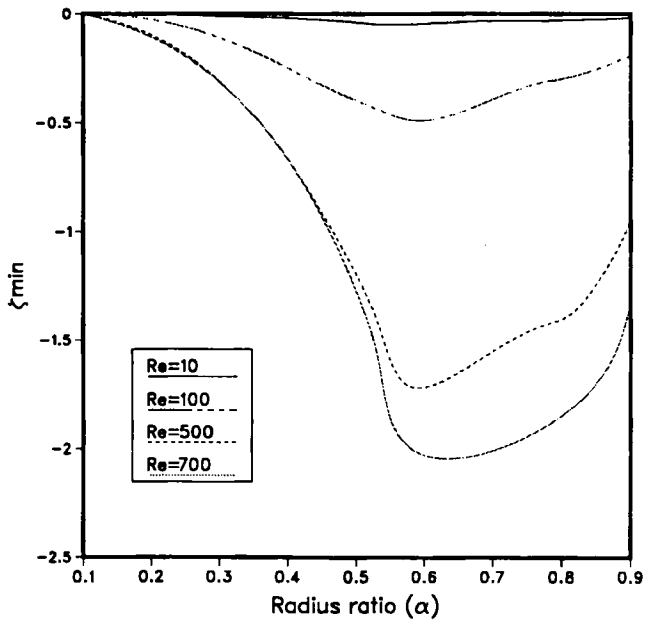

Figure 17. ζ_{min} versus α

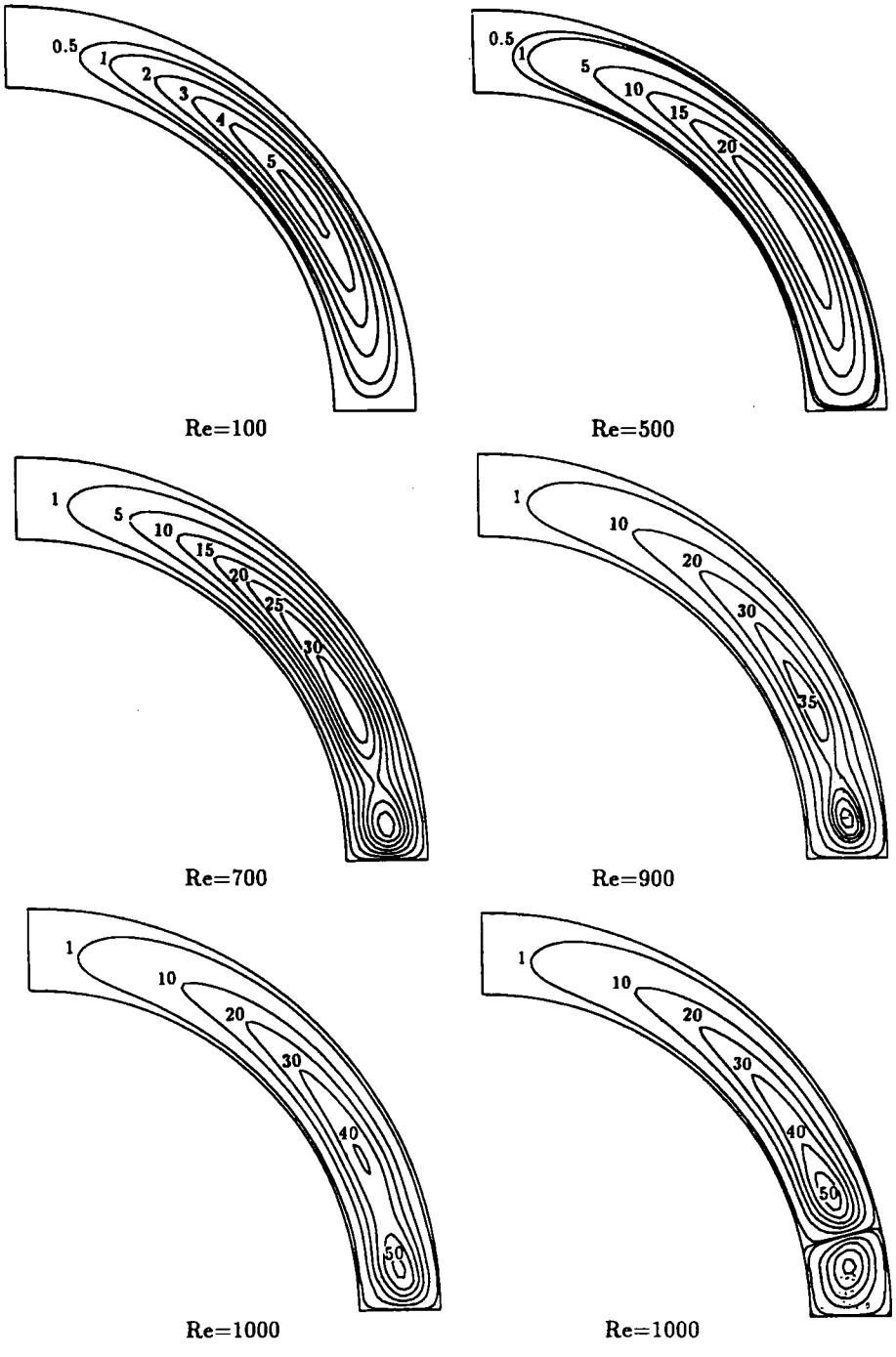

Figure 18. Contour plots of Ψ ($-\Psi \times 10^4$) for $\alpha = 0{\cdot}8$

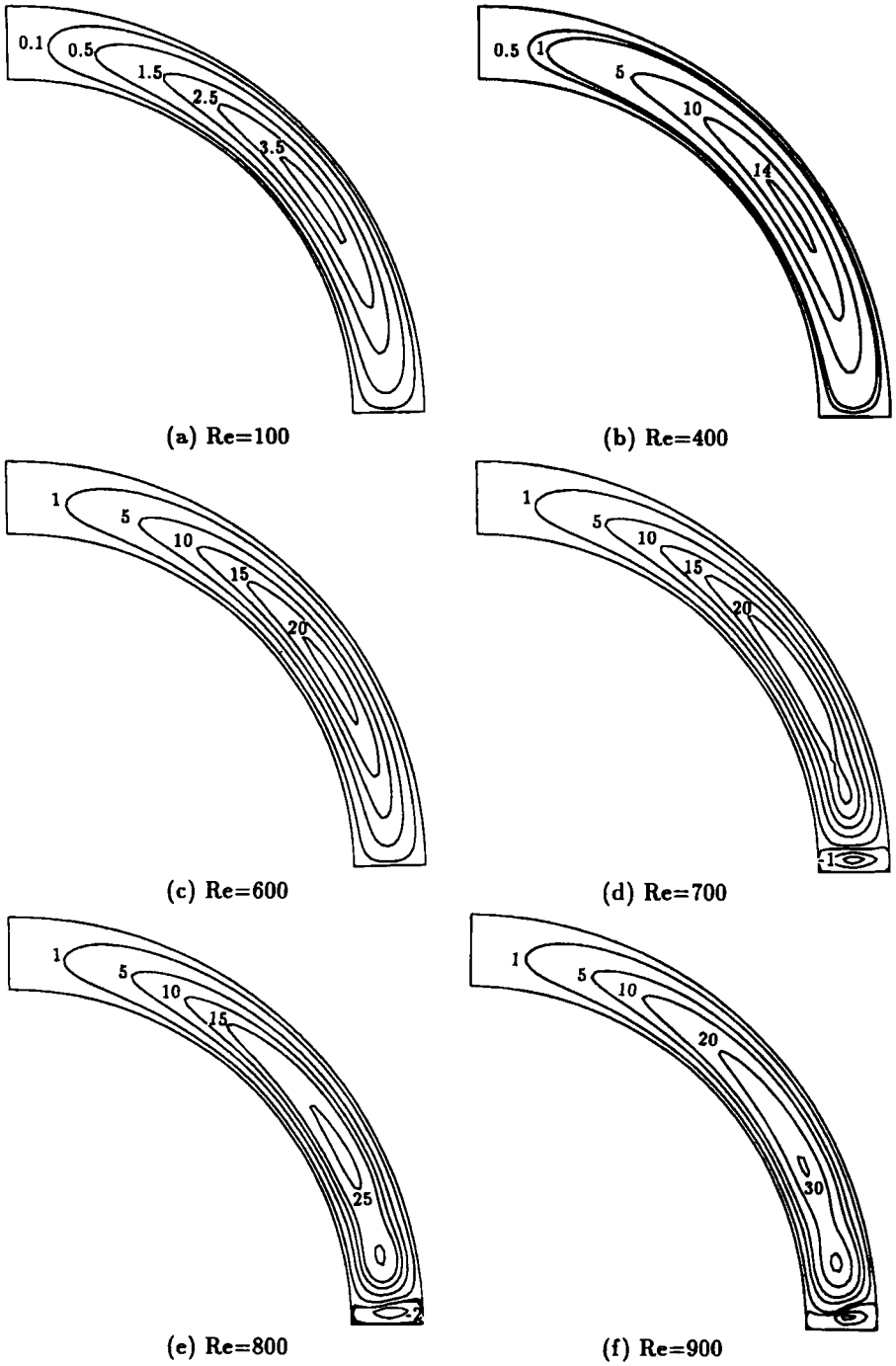

Figure 19. Contour plots of Ψ ($-\Psi \times 10^4$) for $\alpha = 0{\cdot}825$

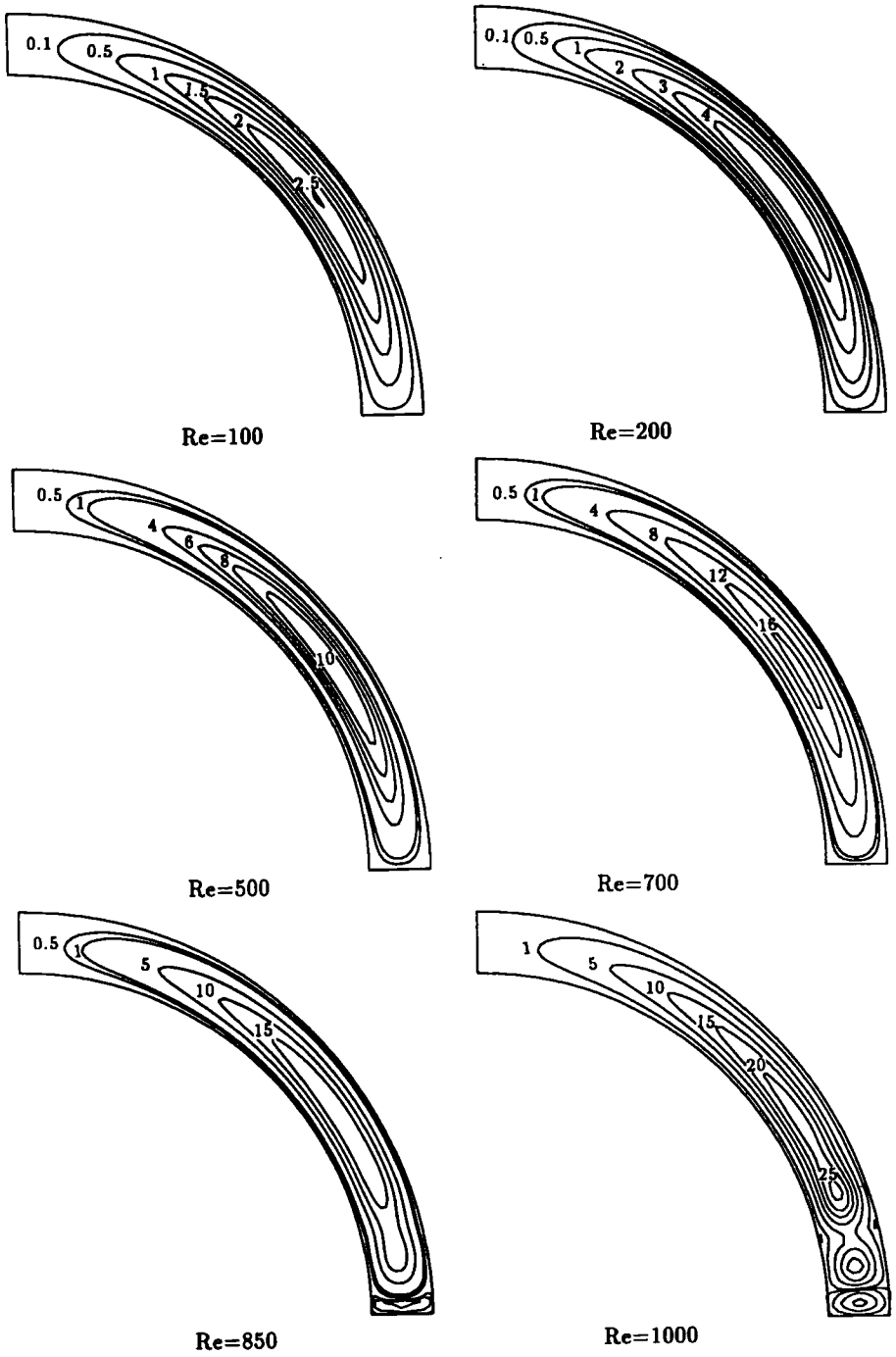

Figure 20. Contour plots of Ψ ($-\Psi \times 10^4$) for $\alpha = 0{\cdot}85$

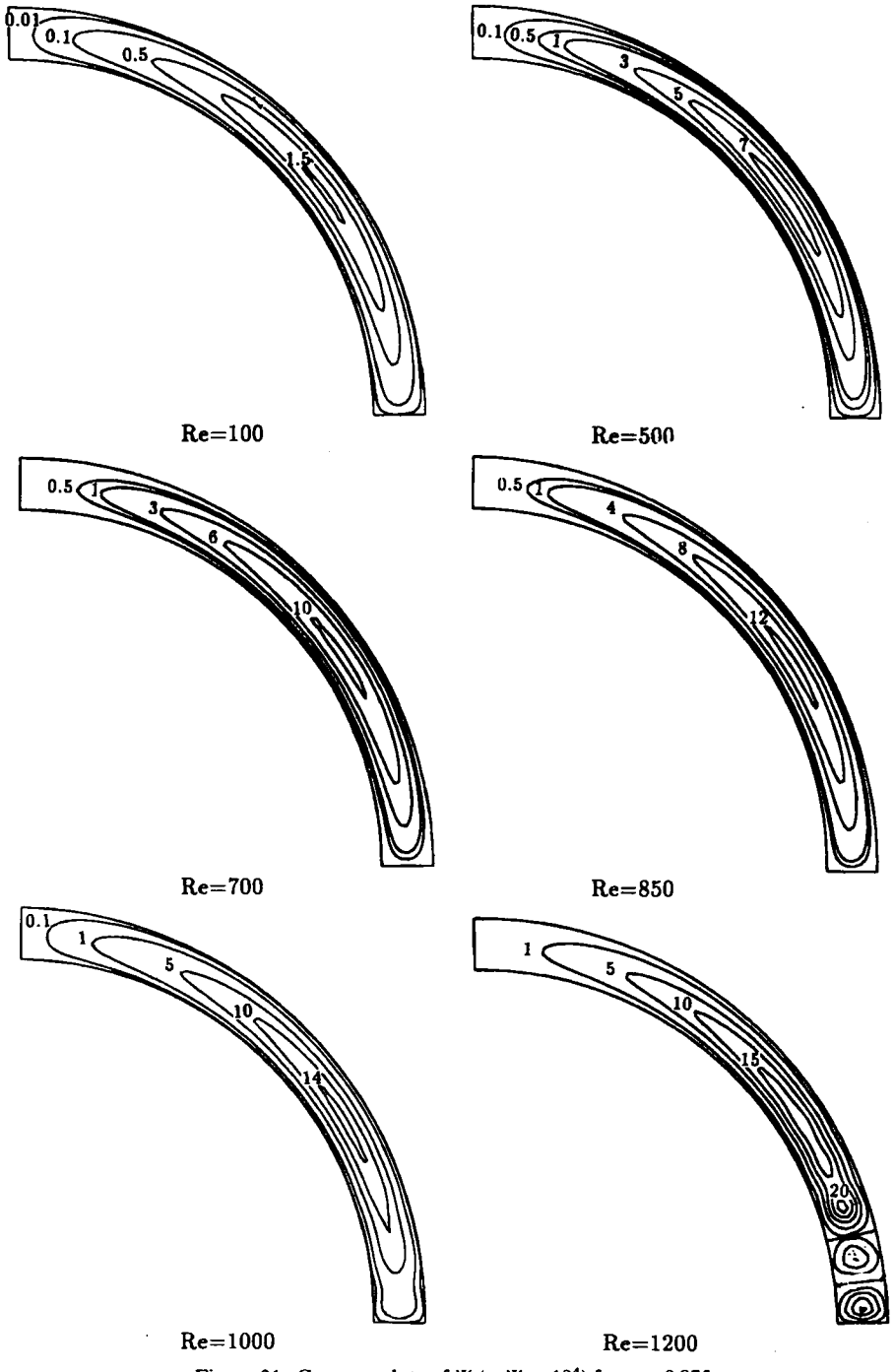

Figure 21. Contour plots of Ψ ($-\Psi \times 10^4$) for $\alpha = 0{\cdot}875$

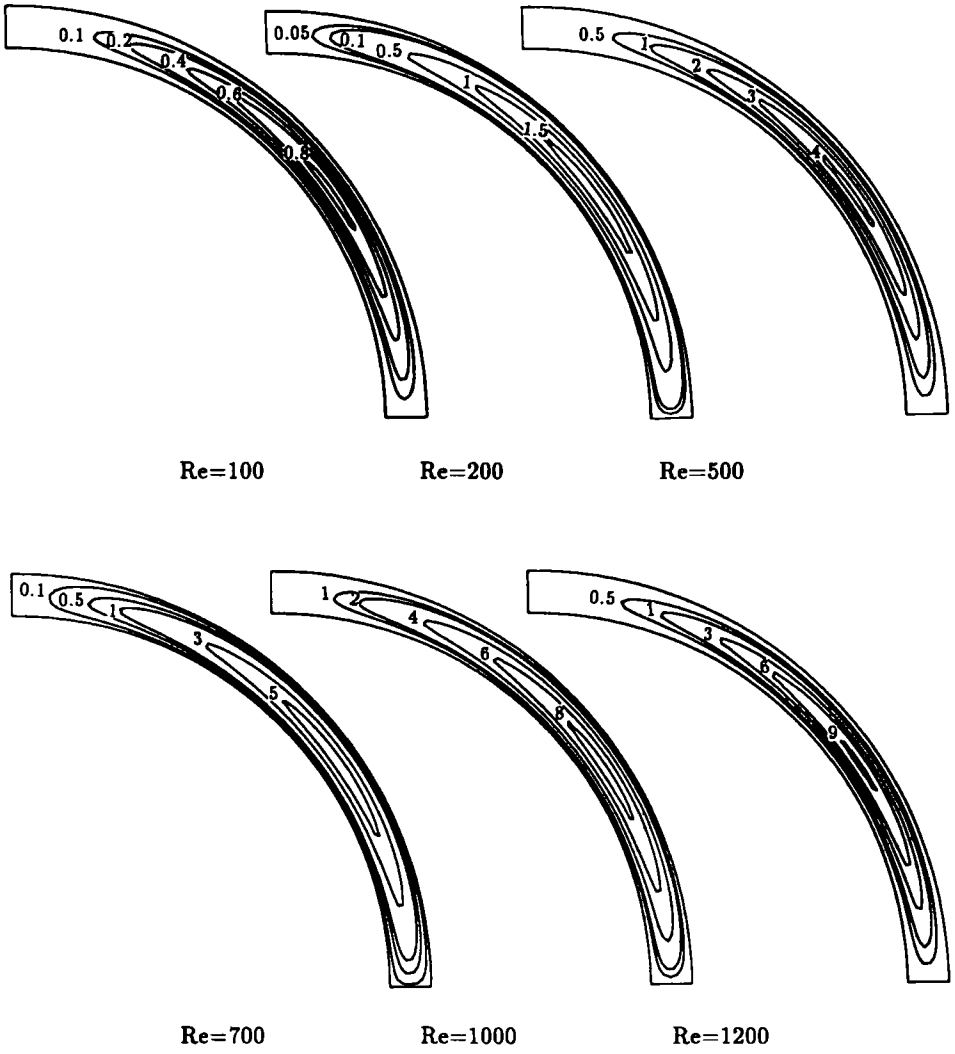

Figure 22. Contour plots of Ψ ($-\Psi \times 10^4$) for $\alpha = 0{\cdot}9$

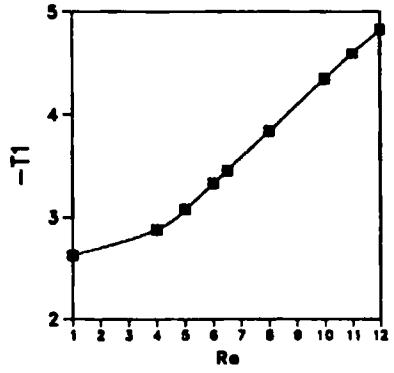

(a) α =0.775

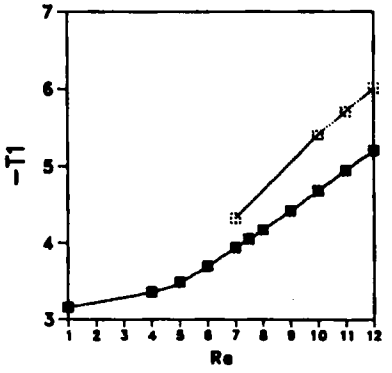

(b) α = 0.8

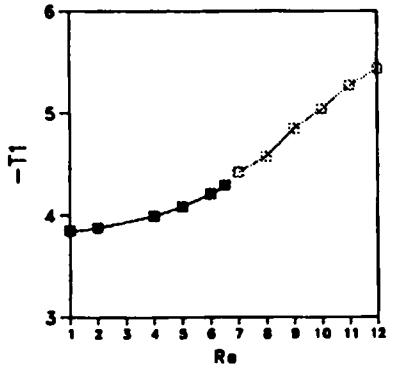

(c) α =0.825

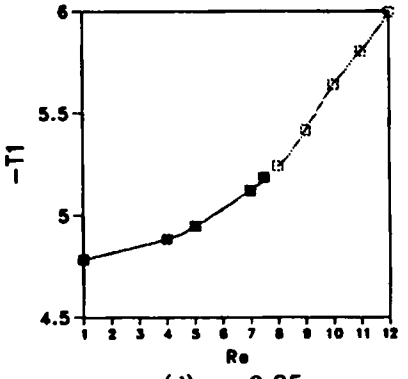

(d) α =0.85

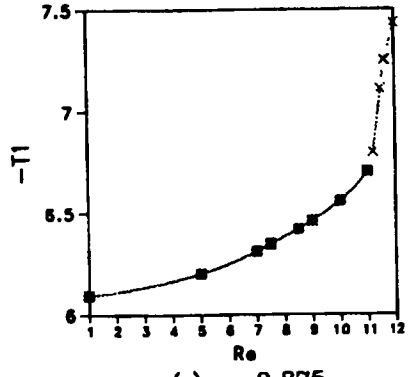

(e) α =0.875

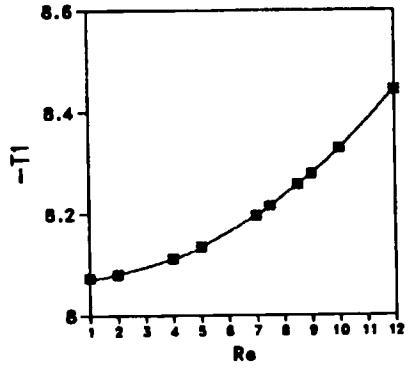

(f) α =0.9

Figure 23. Torque (T_1) versus Reynolds number ($Re \times 10^{-3}$): ■. zero vortex; □, one vortex; ×, two vortices

CONCLUSIONS

The primary objective of this research was to study the use of a modified Galerkin finite element method to analyse the steady state flow of a fluid contained between two concentric, rotating spheres. This method does not require the existence of a potential function to formulate the finite element equations or that the field equations be amenable to integration by parts as in the case of the conventional Galerkin method. The method yielded good results for a wide range of Reynolds numbers and radius ratios. In general the accuracy of the results increased with decreasing mesh size; however, it was important that the aspect ratio be maintained near unity. Future research will be conducted by employing this method to analyse the transient fluid flow problem and problems with non-spherical cavities.

REFERENCES

1. M. P. Sorokin, G. N. Khlebutin and G. F. Shaidurov, 'Study of the motion of a liquid between two rotating spherical surfaces', *J. Appl. Mech. Tech. Phys.*, 7, (6), 73–74 (1966).
2. G. N. Khlebutin, 'Study of fluid motion between a rotating and a stationary concentric sphere', *Fluid Dyn.*, **3**, (6), 31–32 (1968).
3. J. Zierep and Q. Sawatzki, 'Three dimensional instabilities and vortices between two rotating spheres', *Proc. Eighth Symp. on Naval Hydrodynamics*, 1970, pp. 275–288.
4. B. R. Munson and Menguturk, 'Viscous incompressible flow between concentric rotating spheres. Part 3. Linear stability and experiments', *J. Fluid Mech.*, **69**, 705–719 (1975).
5. M. Wimmer, 'Experiments on a viscous flow between concentric rotating spheres', *J. Fluid Mech.*, **78**, 317–335 (1976).
6. M. Wimmer, 'Experiments on the stability of viscous flow between two concentric rotating spheres', *J. Fluid Mech.*, **103**, 117–131 (1981).
7. K. Buhler, 'Symmetric and asymmetric Taylor vortex flow in spherical gaps', *Acta Mech.*, **81**, 3–38 (1990).
8. K. Buhler, 'Dynamical behavior of instabilities in spherical gap flows: theory and experiment', *Eur. J. Mech. B/Fluids*, **10**, 187–192 (1991).
9. I. M. Yavorskaya, Yu. N. Belyaev and A. A. Monachov, 'Investigation of the stability and secondary flows in rotating spherical fluid layers Rossby numbers', *Dokl. Akad. Nauk*, **237**, 804 (1977) (in Russian).
10. K. Nakabayashi, 'Frictional moment of flow between two concentric spheres, one of which rotates', *J. of Fluid Eng.*, **100**, 97–106 (1978).
11. A. M. Waked and B. R. Munson, 'Laminar–turbulent flow in a spherical annulus', *J. Fluid Eng.*, **100**, 281–286 (1978).
12. A. M. Waked and B. R. Munson, 'Torque characteristics for spherical annulus flow', *J. Fluid Eng.*, **101**, 284–286 (1979).
13. I. Proudman, 'The almost-rigid rotation of viscous fluid between concentric spheres', *J. Fluid Mech.*, **1**, 505–516 (1956).
14. K. Stewartson, 'On almost rigid rotation. Part 2', *J. Fluid Mech.*, **26**, 131–144 (1966).
15. G. F. Carrier, 'Some effects of stratification and geometry in rotating fluids', *J. Mech.*, **23**, 145–172 (1965).
16. B. R. Munson and D. D. Joseph, 'Viscous incompressible flow between concentric rotating spheres. Part 1. Basic flow', *J. Fluid Mech.*, **49**, 289–303 (1971).
17. J. C. Gagliardi, N. J. Nigro, A. F. Elkouh, J. Yang and L. S. J. Rodriguez, 'Study of axially symmetric motion of an incompressible viscous fluid between two concentric rotating spheres', *Int. j. numer. methods fluids*, **10**, 1–23 (1990).
18. W. C. Haberman, 'Secondary flow about a sphere rotating in a viscous liquid inside a coaxial rotating spherical container', *Phys. Fluids*, **5**, 625–626 (1962).
19. L. P. Landau and E. M. Lifshitz, *Fluid Dynamics*, Pergamon, New York 1959, p. 68.
20. S. C. R. Dennis and S. N. Singh, 'Calculation of flow between two rotating spheres by the method of series truncation', *J. Comput. Phys.*, **28**, 297–314 (1978).
21. S. D. Gulwadi and A. F. Elkouh, 'Unsteady flow in an annulus between two concentric rotating spheres', *Appl. Sci. Res.*, **49**, 147–159 (1992).
22. P. S. Marcus and L. S. Tuckerman, 'Simulation of flow between concentric rotating spheres. Part 1. Steady states', *J. Fluid Mech.*, **185**, 1–30 (1987).
23. P. S. Marcus and L. S. Tuckerman, 'Simulation of flow between concentric rotating spheres. Part 2. Transitions', *J. Fluid Mech.*, **185**, 31–65 (1987).
24. C. E. Pearson, 'A numerical study of the time dependent viscous flow between two rotating spheres', *J. Fluid Mech.*, **28**, 323–336 (1967).
25. C. E. Pearson, 'A numerical method for incompressible viscous flow problem in a spherical geometry', in *Studies in Numerical Analysis I*, SIAM, Philadelphia, PA, 1968, pp. 65–78.
26. D. Greenspan, 'Numerical studies of steady, viscous, incompressible flow between two rotating spheres', *Comput. Fluids*, **3**, 68–82 (1975).

27. D. Schultz and D. Greenspan, 'Improved solution of steady, viscous, incompressible flow between two rotating spheres', *Comput. Fluids*, **7**, 157–163 (1979).
28. G. Schrauf, 'Branching of Navier–Stokes equations in a spherical gap', *Lecture Notes Phys.*, **170**, 474–480 (1982).
29. S. C. R. Dennis and L. Quartapelle, 'Finite difference solution to the flow between two rotating spheres', *Comput. Fluids*, **12**, 79–92 (1984).
30. S. Schwengels, D. Schultz and W. Shay, 'Second-order finite difference solutions for the flow between rotating concentric spheres', *Int. j. numer. methods in fluids*, **9**, 1099–1111 (1989).
31. E. Krause and F. Bartels, 'Finite-difference solution of Navier–Stokes equations for axially symmetric flow in spherical gaps', *Lecture Notes Math.*, **771**, 313–322 (1979).
32. J. Yang, N. J. Nigro, A. F. Elkouh and J. C. Gagliardi, 'Numerical study of axially symmetric motion of an incompressible viscous fluid between two concentric rotating spheres', *Int. j. numer. methods fluids*, **9**, 689–712 (1989).
33. J. J. Lin, 'A numerical method for solving the motion of an incompressible viscous fluid between two rotating and precessing spheres', *Ph.D. Dissertation*, Marquette University, Milwaukee, WI, 1989.
34. A. J. Baker, 'Finite element theory for viscous fluid dynamics', *Bell Aerospace Co. Res. Rep. 9500-920189*, Buffalo, NY, 1970.
35. A. J. Baker, 'Finite element solution algorithm for viscous incompressible fluid dynamics', *Int. j. numer. methods eng.*, **6** (1973).
36. A. J. Baker, 'A finite element algorithm for the Navier–Stokes equations', *NASA CR-2391*, 1973.
37. R. T. Cheng, 'Numerical solution of the Navier–Stokes equations by the finite element method', *Phys. Fluids*, **15** (1972).
38. T. J. Chung and J. N. Chiou, 'Analysis of unsteady compressible boundary layer flow via finite elements', *Comput. Fluids*, **4**, 1–12 (1976).
39. J. T. Oden, *Finite Elements of Nonlinear Continua*, McGraw-Hill, New York, 1972.
40. J. T. Oden, *Introduction to Mathematical Theory of Finite Elements*, Wiley, New York, 1976.
41. J. T. Oden and C. Wellford, Jr., 'Analysis of flow of viscous flow by the finite element method', *AIAA J.*, **10** (1972).
42. T. J. Oden, O. C. Zienkiewicz, R. H. Gallagher and C. Taylor (eds), *Proc. Int. Symp. on Finite Element Methods in Flow Problems*, Swansea, January 1974, University of Alabama Press, Huntsville, AL, 1974.
43. M. E. Olson, 'Formulation of a variational principle finite element method for viscous flows', *Proc. Conf. on Variational Methods in Engineering*, Southampton, 1972, pp. 5.27–5.38.
44. A. J. Baker, *Finite Element Computational Fluid Mechanics*, McGraw-Hill, New York, 1983.
45. C. A. J. Fletcher, *Computational Galerkin Methods*, Springer, New York, 1984.
46. K. H. Huebner, *The Finite Element Methods for Engineers*, Wiley, New York, 1982.
47. P. Bar-Yoseph, J. J. Blech and A. Solan, 'Finite element solution of the Navier–Stokes equation in rotating flow', *Int. j. numer. methods eng.*, **17**, 1123–1146 (1981).
48. W. Ni and N. J. Nigro, 'Finite elements analysis of the axially symmetric motion of an incompressible viscous fluid in a spherical annulus', *Ph.D. Dissertation*, Marquette University, Milwaukee, WI, 1993.